

Accuracy Issues for Numerical Waveforms

Yosef Zlochower,¹ Marcelo Ponce,^{2,3} and Carlos O. Lousto¹

¹*Center for Computational Relativity and Gravitation,
and School of Mathematical Sciences, Rochester Institute of Technology,
85 Lomb Memorial Drive, Rochester, New York 14623*

²*Center for Computational Relativity and Gravitation,
Technology, 85 Lomb Memorial Drive, Rochester, New York 14623*

³*Department of Physics, University of Guelph, Guelph, Ontario N1G 2W1, Canada*

We study the convergence properties of our implementation of the *moving punctures* approach at very high resolutions for an equal-mass, nonspinning, black-hole binary. We find convergence of the Hamiltonian constraint on the horizons and the L_2 norm of the Hamiltonian constraint in the bulk for sixth- and eighth-order finite difference implementations. The momentum constraint is more sensitive, and its L_2 norm shows clear convergence for a system with consistent sixth-order finite differencing, while the momentum and BSSN constraints on the horizons show convergence for both sixth- and eighth-order systems. We analyze the gravitational waveform error from the late inspiral, merger, and ringdown. We find that using several lower-order techniques for increasing the speed of numerical relativity simulations actually lead to apparently nonconvergent errors. Even when using standard high-accuracy techniques, rather than seeing clean convergence, where the waveform phase is a monotonic function of grid resolution, we find that the phase tends to oscillate with resolution, possibly due to stochastic errors induced by grid refinement boundaries. Our results seem to indicate that one can obtain gravitational waveform phases to within 0.05 rad. (and possibly as small as 0.015 rad.), while the amplitude error can be reduced to 0.1%. We then compare with the waveforms obtained using the CCZ4 formalism. We find that the CCZ4 waveforms have larger truncation errors for a given resolution, but the Richardson extrapolation phase of the CCZ4 and BSSN waveforms agrees to within 0.01 rad., even during the ringdown.

PACS numbers: 04.25.dg, 04.30.Db, 04.25.Nx, 04.70.Bw

I. INTRODUCTION

Numerical relativity (NR) has progressed rapidly since the breakthroughs of 2005 [1–3] that allowed for the long-term evolution of black-hole binaries (BHBs). Among NR’s significant achievements are its contributions towards the modeling of astrophysical gravitational wave sources that will be relevant for the first direct detection and parameter estimation by gravitational wave observatories [4, 5]. NR has also made contributions to the modeling of astrophysical sources, notably, the modeling of the recoil kick imparted to the remnant BH from a BHB merger due to unequal masses [6–8], the remarkable discovery of unexpectedly large recoil velocities from the merger of certain spinning BHBs [9–26, 26–29], and the application of the numerical techniques to combined systems of BHs and neutron stars [30–38]. More mathematical aspects of relativity have also recently been investigated, including the evolution of N-black holes [39–41], the exploration of the no-hair theorem [42, 43], and cosmic [44] and topological censorship [45], as well as BHBs in dimensions higher than four [46–48]. The current state of the art simulations can simulate BHBs with mass ratios as small as $q = 1/100$ [49, 50] and highly spinning BHBs with intrinsic spins $\alpha = S_H/M_H^2$ up to (at least) 0.97 [51, 52]. Currently these runs are very costly and it is hard to foresee the possibility of completely covering the parameter space densely enough for match filtering the data coming from advanced laser interferometric detectors by the time they become operational.

To reduce the computational costs, several low-accuracy approximations are sometimes used. Among them are the techniques introduced in Ref. [53] where the number of buffer zones at AMR boundaries is reduced by lowering the order of finite differencing by successive orders near the AMR boundaries, the use of simple interpolations of spectral initial data rather than using the complete spectral expansion [54], and copying the initial data to the two past time levels for use in prolongation at the initial timestep. All of these approximations proved to be useful for numerical simulations, but each one also has the side effect of introducing a (hopefully) small $\mathcal{O}(h)$ error. In this paper, we examine the effects of these approximations by performing high-resolution simulations of equal-mass, nonspinning BHBs, a problem generally considered well under control. We show that a nonconvergent error, that cannot be detected by simple means, is present when these techniques are used together. However, even when low-accuracy approximations are eliminated, an apparently stochastic error in the waveform phase is still present that prevents us from seeing clean convergence of the waveform even at very high resolutions. We estimate this stochastic phase error is controllable to within NINJA and NRAR accuracy requirements, but does make it very difficult to get an unambiguous measurement of the waveform phase and phase error.

Here we examine in detail the case of a nonspinning equal-mass binary. The idea is that, any issues of accuracy found for these simple systems will only be com-

TABLE I: Initial data parameters. All runs used the same parameters. The punctures are located at $\vec{r} = \pm(x, 0, 0)$, with momenta $\pm(p_r, p_t, 0)$, puncture mass parameters m_p , and zero spin. The ADM mass is 1.00000003. We use $N_{\text{colo.}} \times N_{\text{colo.}} \times N_{\text{colo.}}$ collocation points for the TWOPUNCTURES spectral solver.

x	4.250	m_p	0.4887922277	p_r	-0.00114088
p_t	0.11081837	$N_{\text{colo.}}$	40	M_H	0.50580

pounded by the introduction of different mass ratios (which may require more AMR refinement levels and have a lower effective resolution) and spins (which reduces the smoothness of the data and leads to more complicated motion of the binary).

II. NUMERICAL RELATIVITY TECHNIQUES

To compute the numerical initial data, we use the puncture approach [55] along with the TWOPUNCTURES [54] thorn (see Table I for the initial data parameter). In this approach the 3-metric on the initial slice has the form $\gamma_{ab} = (\psi_{BL} + u)^4 \delta_{ab}$, where ψ_{BL} is the Brill-Lindquist conformal factor, δ_{ab} is the Euclidean metric, and u is (at least) C^2 on the punctures. The extrinsic curvature is given by $K_{ij} = (\psi + u)^{-2} \hat{K}_{ij}$, where \hat{K}_{ij} is a superposition of Bowen-York solution [56] for BHs with spin \vec{S} (here zero) and momentum \vec{p} . The Brill-Lindquist conformal factor is given by $\psi_{BL} = 1 + \sum_{i=1}^n m_i^p / (2|\vec{r} - \vec{r}_i|)$, where n is the total number of “punctures”, m_i^p is a parameter (not the horizon mass), and \vec{r}_i is the coordinate location of puncture i . We evolve these BHB data sets using the LAZEV [57] implementation of the moving puncture approach [2, 3] with the conformal function $W = \sqrt{\chi} = \exp(-2\phi)$ suggested by Ref. [58] (where χ is the evolution variable introduced in [2]). The moving puncture approach is based on the Baumgarte-Shapiro-Shibata-Nakamura (BSSN, BSSN-NOK) formalism [59–61], where the gauge and evolution variables are adapted such that the system is finite at the punctures. For the runs presented here, we use centered, eighth-order finite differencing in space [39] and a fourth-order Runge Kutta time integrator. (Note that we do not upwind the advection terms.) For points near (but not on) the computational domain boundary, we reduce the order of finite differencing such that the stencils fit in the computational domain (i.e. reduce from eighth to sixth to fourth to second).

On the boundary points themselves, we use radiative boundary conditions for all variables, which on the $x = x_{\text{min}}$ and $x = x_{\text{max}}$ faces, have the form

$$\partial_t f|_x = -v \left(\frac{r}{x} \partial_x f + \frac{f - f_\infty}{r} \right), \quad (1)$$

where the wavespeed v and asymptotic value of the function f_∞ are parameters. We set the wavespeed to 1

for $\tilde{\gamma}_{ij}$, \tilde{A}_{ij} , and β^i , while we set the wavespeed to $\sqrt{2}$ for α , K , and W . We calculate $\partial_x f$ using a one-sided, second-order stencil. We set $f_\infty = 0$ for all variables except $\tilde{\gamma}_{ii}$, α and W , where we set $f_\infty = 1$.

In the *method of lines* approach, for every evolved function f , there is a corresponding function f_{RHS} , where $\partial_t f = f_{\text{RHS}}$. The evolution code fills in all the RHS grid-functions (including on the boundaries). No additional boundary conditions (except symmetry boundary conditions) are applied to the evolution variables themselves.

After each *substep* of the RK4 integration, we enforce the algebraic constraints, $\tilde{\gamma} = \det(\tilde{\gamma}_{ij}) = 1$ and $\tilde{A} = \tilde{\gamma}^{ij} \tilde{A}_{ij} = 0$ by renormalizing $\tilde{\gamma}_{ij}$ and subtracting the trace from \tilde{A}_{ij} , i.e.

$$\tilde{\gamma}_{ij} \rightarrow \frac{1}{\tilde{\gamma}^3} \tilde{\gamma}_{ij},$$

and

$$\tilde{A}_{ij} \rightarrow \tilde{A}_{ij} - \frac{1}{3} \tilde{\gamma}_{ij} \tilde{A}.$$

Our code uses the CACTUS/EINSTEINTOOLKIT [62–64] infrastructure. We use the CARPET [65] mesh refinement driver to provide a “moving boxes” style of mesh refinement. In this approach refined grids of fixed size are arranged about the coordinate centers of both holes. The CARPET code then moves these fine grids about the computational domain by following the trajectories of the two BHs.

We use AHFINDERDIRECT [66] to locate apparent horizons. We measure the magnitude of the horizon spin using the Isolated Horizon algorithm detailed in Ref. [67]. Note that once we have the horizon spin, we can calculate the horizon mass via the Christodoulou formula

$$m^H = \sqrt{m_{\text{irr}}^2 + S_H^2 / (4m_{\text{irr}}^2)}, \quad (2)$$

where $m_{\text{irr}} = \sqrt{A / (16\pi)}$ and A is the surface area of the horizon (we neglect the effects of momentum).

For the gravitational waveform, we calculate the Newman-Penrose ψ_4 Weyl scalar using fourth-order centered finite differencing and then decompose ψ_4 at fixed radii using spin-weighted spherical harmonics, $\psi_r = \sum_2^N c_{\ell, m-2} Y_{\ell m}$. We use a fourth-order accurate integration to calculate the (ℓ, m) modes of ψ_4 . We also calculate the Hamiltonian (\mathcal{H}), momentum (\mathcal{C}^i), and BSSN constraint (\mathcal{G}^i) violations using fourth-order centered finite differencing. We use fourth-order finite differencing to reduce the computational cost of calculating analysis quantities.

For our gauge conditions, we use a modified 1+log lapse and a modified Gamma-driver shift condition [2, 68, 69], and an initial lapse $\alpha(t=0) = 2 / (1 + \psi_{BL}^4)$. The lapse and shift are evolved with

$$(\partial_t - \beta^i \partial_i) \alpha = -2\alpha K, \quad (3a)$$

$$\partial_t \beta^a = (3/4) \tilde{\Gamma}^a - \eta \beta^a, \quad (3b)$$

where we use $\eta = 2$ for all simulations presented below.

For our tests of the fast, but low-accuracy techniques, we performed a set of 11 simulations. In all cases, the physical boundaries of our computational domains were located at $400M$ in all coordinate directions, although we did use π -symmetry and z -reflection symmetry to reduce the computational domain by a factor of 4. We chose configurations with a base outer resolution of $h_0 = 400M/70$ with 9 levels of refinement. The finest resolution was $M/44.8$. We then used global refinements of this base configuration with outer resolutions of $h_1 = 400M/84$, $h_2 = 400M/100$, and $h_3 = 400M/120$. The ratio between the timestep and spatial resolution on the coarsest grid was set to 0.06125, the next two levels had $1/2$ this timestep, the following three had $1/4$, and then each additional level had time refinement of a factor of 2 with respect to the next coarsest grid. The ratio κ of the timestep and spatial resolution [Courant factor (CFL)] on the finest timelevel was $\kappa = dt/h = 0.49$. In addition, we performed simulations with all CFL factors reduced by factors of 2, $2\sqrt{2}$, and 4. For the low accuracy study we used the reduction of order technique proposed in [53] to reduce the number of buffer zones at the refinement boundaries to six. This is accomplished using the following algorithm. During the four Runge-Kutta substeps, we used the largest centered finite differences stencil located within a given AMR level (including buffer zones), i.e., for interior points at least 4 points from the AMR boundaries (in all direction), we used standard eighth-order finite differencing, while for points closer to the AMR boundaries, we used progressively lower orders. On the AMR boundaries themselves, we used a simple copy procedure, where data from the previous time level was copied onto the AMR boundary. Then, after the subcycling is complete, we overwrite the AMR boundary points, and an additional 5 points inside the AMR boundary via prolongation. Note that this means that during the four substeps of the RK4 integration, information from the AMR boundaries can propagate outside the buffer region (and hence reduce the order of convergence of the bulk).

To initialize the past timelevels of the initial slice, we used a simple copy. This introduces an $\mathcal{O}(h)$ error in the prolongation of the first time level. Since all subsequent field points depend on the data on this time level, a small $\mathcal{O}(h)$ error should persist throughout the evolution. We also used the `interpolation` option of TWOPUNCTURES to quickly interpolate the spectral solution on the grid. This approximation has the effect of introducing high-frequency noise (which does dissipate away) and constraint violation (which does not).

We performed 25 high-accuracy simulations. For these simulations, we used nearly identical spatial grid structure, but had identical CFL factors on each gridlevel. In addition, we used resolution $h_1 \cdots h_3$ above and a higher resolution $h_4 = 400M/144$ (we also performed a single run with resolution $h_5 = 400M/174$). We used CFL factors of $\kappa = 1/4$, $\kappa = 1/(4\sqrt{2})$, and $\kappa = 1/8$. A CFL

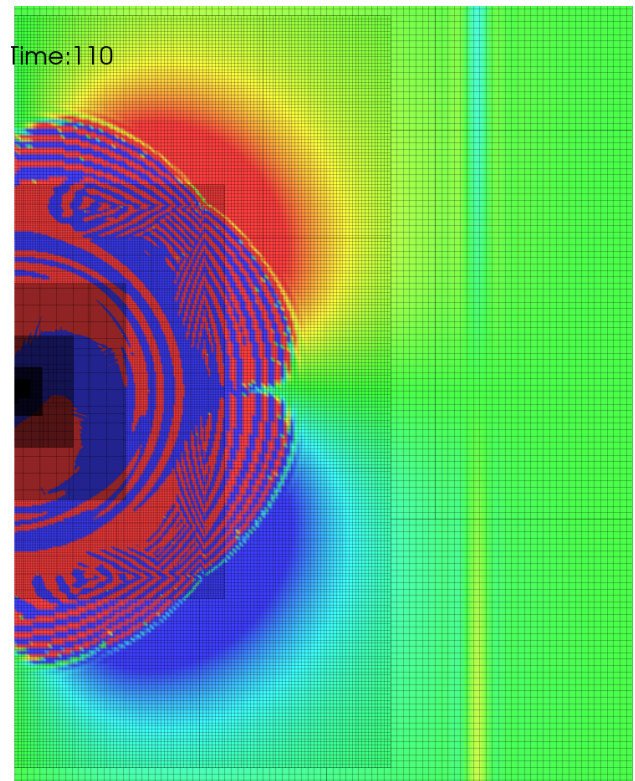


FIG. 1: A plot of the $\Re\{\psi_4\}$ on the xy plane at $t = 110M$. Note the interference pattern that develops as part of the wave reflects off the AMR boundary. Also note that the reflection originates in the buffer region and not on the AMR boundary itself. The reflected waves will soon interfere producing still higher spatial frequencies.

factor of $\kappa = 1/2$ was not stable (due to low-resolution in the outer grid [70]). These runs also differed from the low-accuracy runs in that a full complement of 16 buffer zones were also used and no reduction of order near AMR boundaries was necessary. In addition we used the `init_3.timelevels` algorithm to initialize the grid, which properly initializes the past two timelevels of the initial data slice, and we used the computationally expensive `evaluation` option for TWOPUNCTURES. The final two parameters that determine the accuracy of our simulations are the dissipation order and prolongation order. We found that fifth-order Kreiss-Oliger dissipation was most effective at suppressing the high-frequency noise that originates as reflections from AMR boundaries (see Fig. 1). We similarly used fifth-order prolongation operators. As an additional check, we compare all runs with two other systems, an eighth-order system with seventh-order dissipation and prolongation (we use seventh rather than ninth to reduce the number of required buffer points) and a fully consistent sixth-order system with seventh-order dissipation and prolongation operators.

In the current work, we are interested in computing the phase of the dominant ($\ell = 2, m = 2$) mode of ψ_4 at

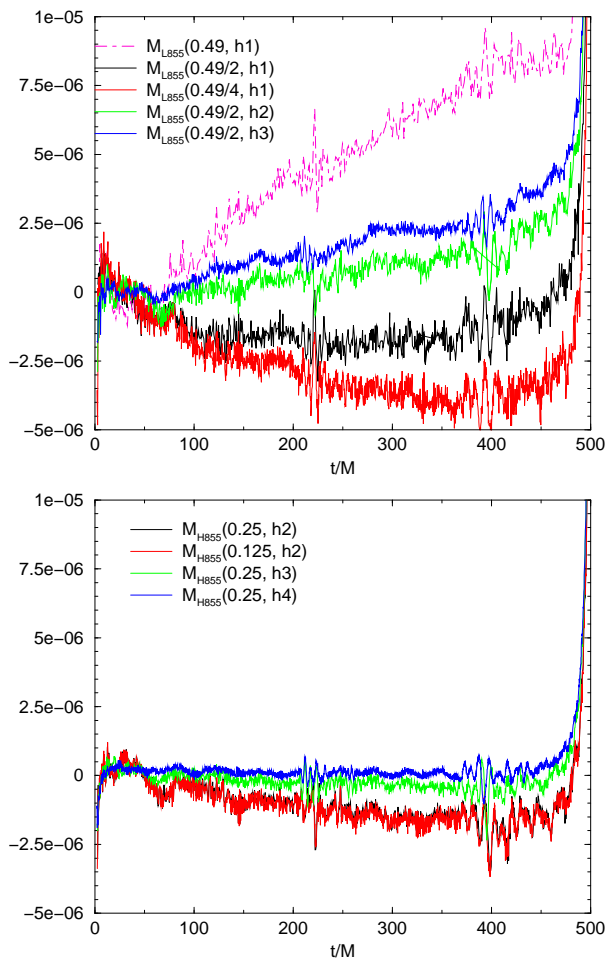


FIG. 2: The horizon mass as a function of time for different resolutions and CFL factors for the L855 algorithm (top) and H855 algorithm (bottom). Note the poor mass conservation for the low accuracy simulations. Also note that the mass for the H855 simulations is unaffected by CFL (i.e. the curves corresponding to different CFLs lie on top of each other), while the mass is strongly affected by CFL for the low accuracy simulations.

finite radius. While there can be significant phase errors associated with extrapolation to $r = \infty$, these errors are controllable by using larger computational domains, multipatch methods [71], pseudospectral methods [72], and Cauchy-Characteristic extraction [73, 74]. Ideally, with high, but still practical, resolution, the phase error in the waveform would be at or below the phase differences inherent in choosing different background metric ansatz for the same binary configuration, which was found to be $< 10^{-2}$ rad. using spectral codes [75].

In the figures and tables below, we denote the low accuracy simulations by “L855” and higher-accuracy simulations by “H855”, “H877”, and “H677”. Here the first digit indicates the spatial finite-difference order, the second indicates the dissipation order, and the third indicates the spatial prolongation order.

TABLE II: Differences between the low-accuracy, and high-accuracy configurations. “N Buffer” is the number of buffer zones at refinement boundaries, “Initial Data” refers to the method used for computing the conformal factor from the spectral coefficients, “AMR Initialization” refers to the order of approximation used to initialize the past time levels of the initial slice (used for prolongation only). Here, “radius” refers to the “half-width” in all directions of each level and CFL refers to the ratio between dt and h on that level. All high-accuracy simulations (H855, H877, H677) use the same grid structures and initialization parameters.

	low	high
N Buffer	6	16
Initial Data	interpolation	evaluation
AMR Initialization	1st order	4th order

	low	high		
level	radius	CFL	radius	CFL
0	400	$\kappa/8$	400	κ
1	208	$\kappa/8$	208	κ
2	115	$\kappa/8$	115	κ
3	60	$\kappa/4$	60	κ
4	30	$\kappa/4$	30	κ
5	12	$\kappa/2$	12	κ
6	5	κ	5	κ
7	1.5	κ	1.5	κ
8	0.75	κ	0.75	κ

III. RESULTS

Our studies were motivated by phase errors in intermediate-mass-ratio simulations [76]. In that study, we found that mass conservation was an important criterion for an accurate evolution. Here we study the conservation of the horizon mass as a function of resolution and CFL factor for both the L855 and H855 configurations.

A. Horizon Mass

The horizon mass for nonspinning BHs is given by the irreducible mass $M_{\text{irr}} = \sqrt{A_H}/16$, where

$$A_H = \oint d^2s, \quad (4)$$

the integral is performed over the surface of the horizon and d^2s is the proper *volume* element on the horizon associated with the induced metric on the horizon. We can also define the horizon average of a function H as

$$\langle H \rangle = \frac{\oint H d^2s}{\oint d^2s}. \quad (5)$$

Similarly, we can describe horizon fluxes of a vector field \mathcal{C}^i with the flux integral

$$\langle \mathcal{C}^i \rangle = \frac{\oint \mathcal{C}^i R_i d^2s}{\oint d^2s}, \quad (6)$$

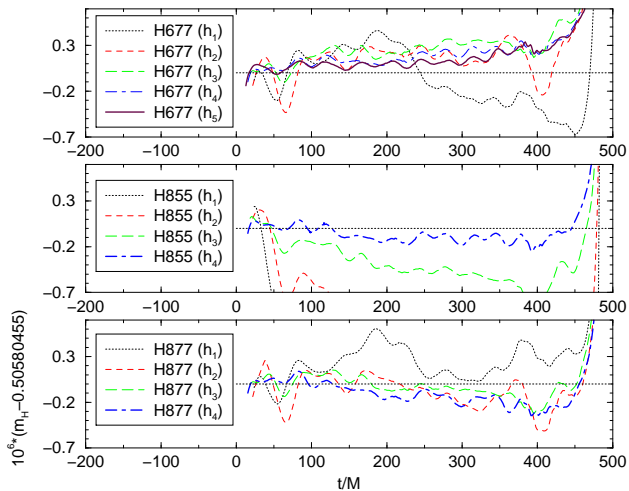


FIG. 3: The horizon mass versus resolution for the H855, H877, and H677 systems (all with CFL=0.25). Here the horizon mass has been smoothed by using a running average. At high resolutions, H855 and H677 both show very flat masses. H855 and H877 both show a small drop in mass, which is unphysical, while H677 shows an increase in mass.

where R_i is the unit norm on the horizon.

As shown in Fig. 2, the conservation of the horizon mass for the L855 simulations is strongly affected by the CFL factor, with the largest deviations being between the $\kappa = 0.49$ and $\kappa = 0.49/4$ CFL factors. On the other hand, for the H855 simulations, the conservation of mass is unaffected by CFL, but is rather affected only by an increase in spatial resolution. Also note that the mass profiles are much flatter in the H855 simulations.

We compare the horizon masses obtained with the H855, H877 and H677 systems (at a fixed CFL of 0.25) in Fig. 3. The H855 shows the most variation with resolution, but appears to be comparable to H877 at high resolution. H855 and H877 both show a small drop in mass, which is unphysical, while H677 shows an increase in mass. At intermediate resolutions, it appears that H877 or H677 are better than H855 in terms of mass conservation. At high resolutions, H855 and H877 appear to be slightly more accurate than H677 since they show flatter profiles of the mass versus time.

B. Constraints

The size of the constraint violations is a measure of how closely the simulations obey the Einstein equations, and, in addition, violations of the constraint can lead to mass loss. We examined the Hamiltonian constraint violation both in the bulk and the average of the Hamiltonian constraint violation on each horizon. The idea of using the horizon average constraints is to see how much *strange* matter is falling into the BHs (and thus a source of mass fluctuation).

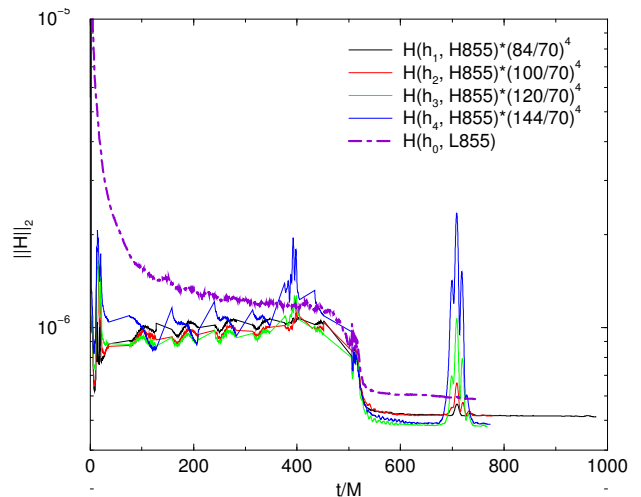


FIG. 4: Convergence of the L_2 norm of the Hamiltonian constraint in the volume between the horizons and a coordinate sphere at $r = 20M$. Fourth-order convergence, consistent with the constraint calculation algorithm (and also the time integrator) is apparent for the H855 simulations. The low accuracy simulation shows a larger error during the inspiral, which may be the source of the error in the simulation. Spikes associated with the BHs crossing the symmetry boundary at $x = 0$, which are an artifact associated with π symmetry, have been removed (see Fig. 5).

As seen in Figs. 4 and 6, the Hamiltonian constraint violation in the bulk is significantly larger for the L855 simulations than the higher accuracy H855 simulations, with the constraint violation appearing immediately at the start of the simulation and decreasing towards the values seen in the H855 simulations. The H855 simulations, on the other hand, show clear fourth-order convergence. The constraints on the horizons converge to fourth-order for the H855 simulations, with similar values to the L855. We can therefore conclude that absorption of constraint violation by the horizon is not the ultimate source of either the lack of conservation in the mass or the phase error in the waveform. Spikes in the L_2 norm of the Hamiltonian, which are an artifact of the π -symmetry (possibly in the way the grids around each BH need to be enlarged near the symmetry boundary, or even an analysis artifact), as shown in Fig. 5, have been removed from Fig. 4. In Fig. 5, we show the the phase difference between a run that uses π -symmetry and one that does not. The differences in the phase are under 0.001 rad. over the entire waveform.

In Figs. 7 and 8, we compare the L_2 norm and horizon-averaged values of the Hamiltonian constraint violations for the H855, H877, and H677 systems (all with CFL 0.25). Unlike the horizon mass, here H855 shows better behavior than H877. That is H855 shows convergence of the L_2 norm to zero, while H877 shows convergence to a finite value. In Fig. 9, we show the L_2 norm of the

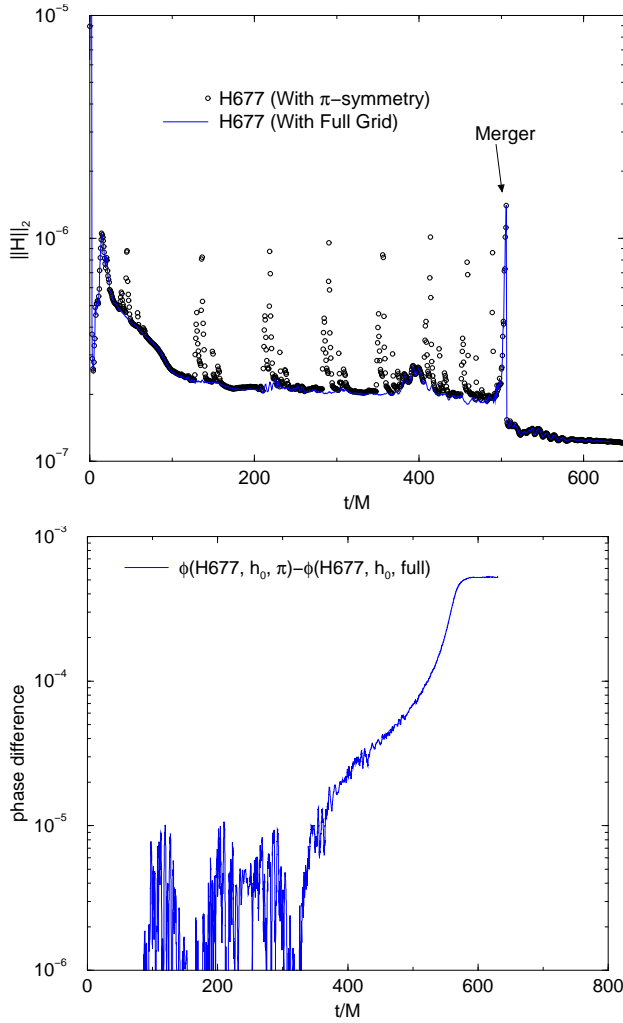


FIG. 5: A plot showing that the spikes in the L_2 norm of the Hamiltonian are an artifact of π -symmetry when the BHs cross the symmetry boundary. The plot shows the L_2 norm for identical runs, with the exception that one does not use π symmetry. Outside the spikes themselves, the two runs agree. The bottom plot shows the phase differences between (otherwise identical) runs with and without π -symmetry.

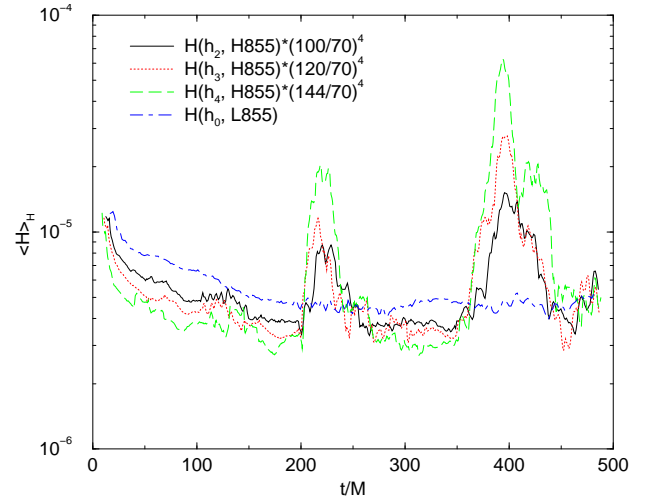


FIG. 6: Convergence of the horizon averaged value of the Hamiltonian constraint violation for the H855 system. The horizon average constraint violation of H855 is consistent with that of L855 (after accounting for differences in resolution).

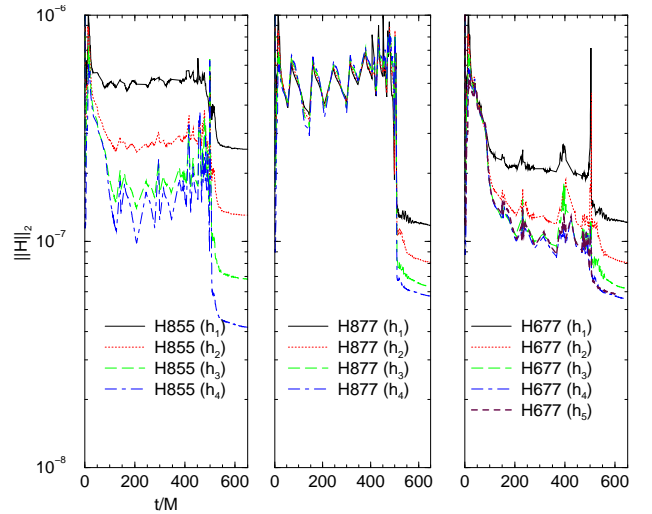


FIG. 7: The L_2 norm of the Hamiltonian constraint for the H855, H877, and H677 systems. H877 shows clear convergence to a finite value at all resolutions. For H855, the constraint decreases with resolution but appears to converge to a smaller finite value. H677 shows the best behavior, but also converges to (a still smaller) finite value. Post merger, H855 gives the smallest violation (but only at the highest resolution). At lower resolution, H855 gives the largest violation. Note that the curves have not been rescaled.

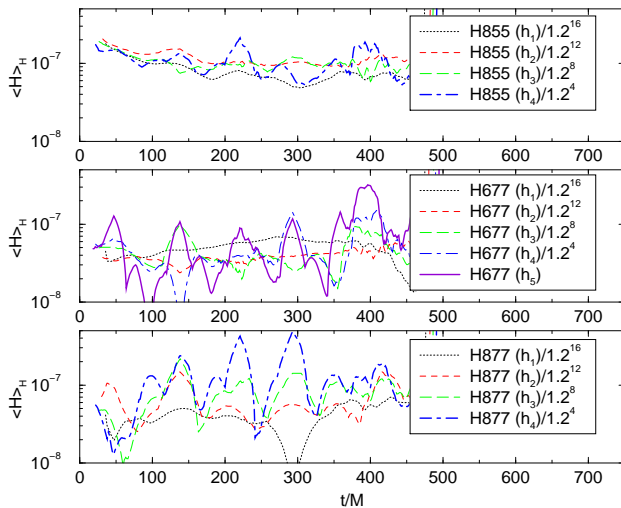


FIG. 8: The horizon average value of the Hamiltonian constraint for the H855, H877, and H677 systems. In all cases, the CFL was set to 0.25. The constraint violation have been rescaled assuming fourth-order convergence. In all cases, convergence to zero is poorest at the highest resolutions. H677 shows the most convergent behavior, while H877 shows the poorest.

x component of the momentum constraint (other components are qualitatively similar). Here, only the H677 simulations show consistent convergence with resolution.

To summarize, at medium resolutions, both H877 and H677 preserve the horizon mass better than H855. At high resolution, H855 appears to be a little better than H877 or H677 (slightly flatter profile). The horizon-averaged constraint violations appear to be smallest for H677, followed by H855. The L_2 norm of the constraint violation favors H677 prior to merger (and after $t = 150M$), and H855 (high resolution) post merger. Prior to $t = 150M$, high resolution H855 is better.

In Fig. 10 we plot the horizon average of the momentum constraint $\langle C^i \rangle_H$ and BSSN constraint $\langle \mathcal{G}^i \rangle_H$, where $\mathcal{G}^i = \tilde{\Gamma}^i + \partial_j \tilde{\gamma}^{i,j}$, which is identically zero if the underlying ADM equations are solved exactly. These two horizon quantities can be thought of as the flux of constraint violation entering the horizons. For the momentum constraints, the three systems seem to have the same level of constraint violation. On the other hand, for the BSSN constraint, the H855 system shows larger constraint violations at all resolutions than the other two.

Based on these results, one may expect that the high-resolution H677 is the most accurate. The horizon-averaged Hamiltonian and momentum constraint (but not BSSN constraint) seem to indicate that the next most accurate simulation, at high resolution, is H855. While it is surprising that H877 does not perform as well as H677, this may be due to effects of reduced dissipation combined with the eighth-order algorithm.

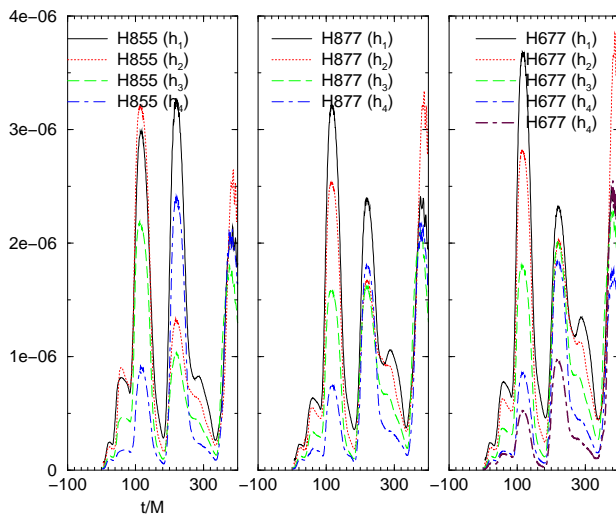


FIG. 9: The L_2 norm of the x -component of the Momentum constraint for the H855, H877, and H677 systems. Only the H677 system shows consistent convergence to zero with resolution. Note that the constraints have not been rescaled.

C. Phase errors

For the L855 configurations we saw clean convergence of the phase of the $(\ell = 2, m = 2)$ mode of ψ_4 (see Fig. 11) at the smallest CFL factor (0.125). While eighth-order convergence in the phase is apparent, the actual phase error is relatively large, when effects of the CFL factor are included. In Fig. 12 we show the convergence of the phase for both the L855 and H855 simulations. Fourth-order convergence is apparent in the H855 simulations.

In Figs. 13 and 14, we show the phase of the $(\ell = 2, m = 2)$ mode of ψ_4 as a function of CFL factor κ . Note that this means that only the timestep is refined, not the spatial resolution. One might expect that the error would decrease, or at least not increase, as dt is made smaller. Generally, this is the case, however, we note that the error can increase as dt is made smaller due to the effects of dissipation. For example, for a simple first-order discretization for the advection equation, at fixed spatial resolution, the error in the solution for a marginally resolved waveform increases as $\kappa \rightarrow 0$. In Fig. 15, we show the convergence of the phase as a function of the CFL factor (at fixed spatial resolution). The L855 simulations show clear first-order convergence at all spatial resolutions, while the H855 simulations actually show an increase in error with CFL at higher resolu-

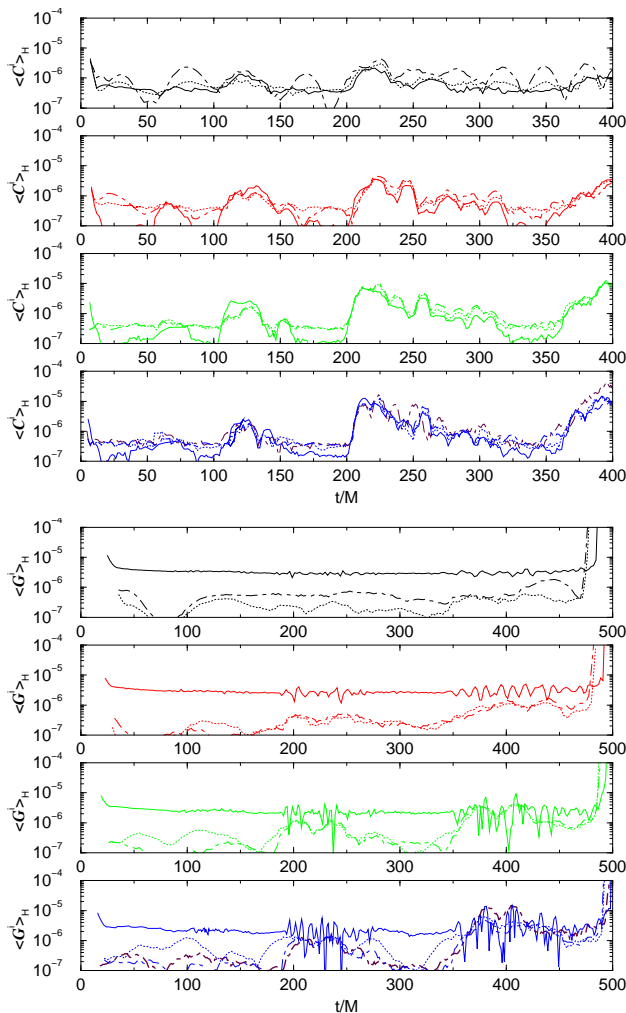


FIG. 10: The horizon momentum constraint flux $\langle C^i \rangle_H$ and BSSN constraint flux $\langle G^i \rangle_H$. Here H677 results are displayed using dot-dashed curves, H877 using dashed curves, and H855 using solid curves. The subplots are stacked by resolution, with h_1 on top, followed by h_2 , h_3 . The bottom subplot shows results for h_4 , as well as h_5 (thick solid line) for H677. Note that both the momentum and BSSN the constraints have been rescaled by a factor of $(h_i/h_5)^4$ (i.e. assuming fourth-order convergence).

The above observed phase oscillations occur, but at a magnified level for non-equal mass systems. In Fig. 16, we show the waveform phase for a $q = 1/10$ BHB evolved using the L855 system with $\kappa = 1/4$ [76].

D. Comparing waveform phases using different dissipation and prolongation operators

In Fig 17, we show the phase of the $(\ell = 2, m = 2)$ mode of ψ_4 near merger for the H855, H877, and H677

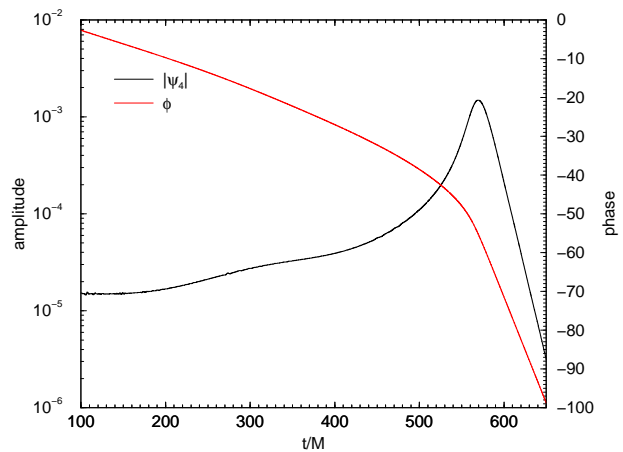


FIG. 11: The magnitude and phase of the $(\ell = 2, m = 2)$ mode of ψ_4 extracted at $r = 50M$. The magnitude is shown on a log scale, while the phase is shown on a linear scale. The exponential decay of the quasinormal ringdown is evident after $t \gtrsim 585M$.

simulations. Combining the information from Figs. 15 and 13, we conclude that the L855 system shows a clear trend where the waveform at infinite resolution is a function of CFL factor. This means that at fixed CFL, which is how numerical convergence studies are performed, there is a nonconvergent, error in the phase. Fortunately, the phase for the H855 simulations appears to be independent of CFL.

systems. *A priori*, we might expect that the H877 systems is the most accurate, and would therefore show the smallest amount of scatter and spurious oscillations of the phase with resolution. In fact, this system, and H677, shows significantly larger scatter than H855. A possible explanation is that the H877 and H677 systems are the least dissipative, and therefore most sensitive to high-frequency grid noise errors (these high frequency signals originate as interference signals from the reflection of the initial data pulse at the AMR boundaries).

The H877 system does not appear to be consistent with

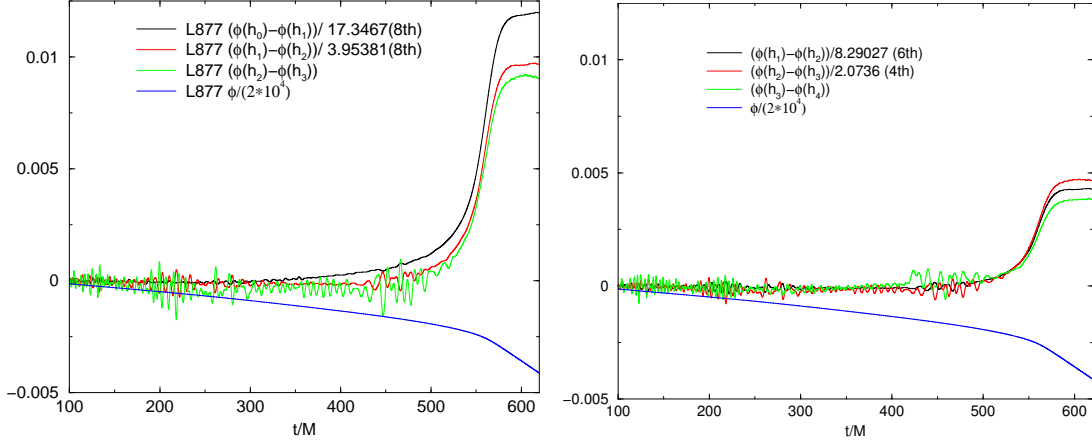


FIG. 12: Convergence of the phase of the $(\ell = 2, m = 2)$ mode of ψ_4 for the L855 (left) and H855 (right) simulations. In all cases the CFL factor was 0.125 on the finest grid. Higher-order convergence is apparent for the L855 system. However, the solution itself has a nonconvergent error.

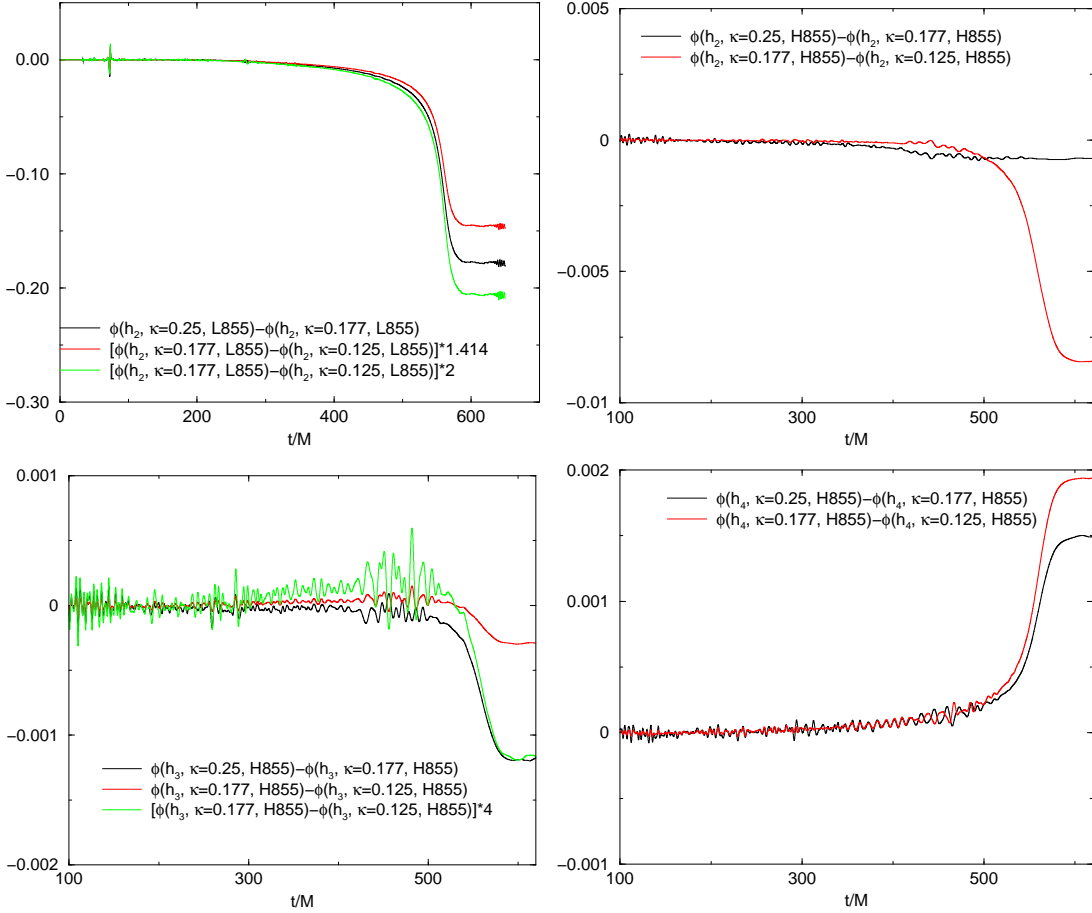


FIG. 13: Convergence of the phase with changes to the CFL factor. The top left panel shows the convergence of the phase for the L855 system. Slightly better than first-order convergence is seen. The top right panel shows the convergence rate, at the same spatial resolution, for the H855 simulations. Note the phase differences are a factor of 10-100 smaller, but not convergent. The bottom left shows the same convergence plot, but for the next higher spatial resolutions. Clean 4th-order convergence is seen at late times, at early times the differences are consistent with zero. Finally, the bottom right panel shows the same plot, but for the highest resolutions runs. Here again, convergence is not observed with CFL. Also the phase differences with CFL are larger than for the medium resolution.

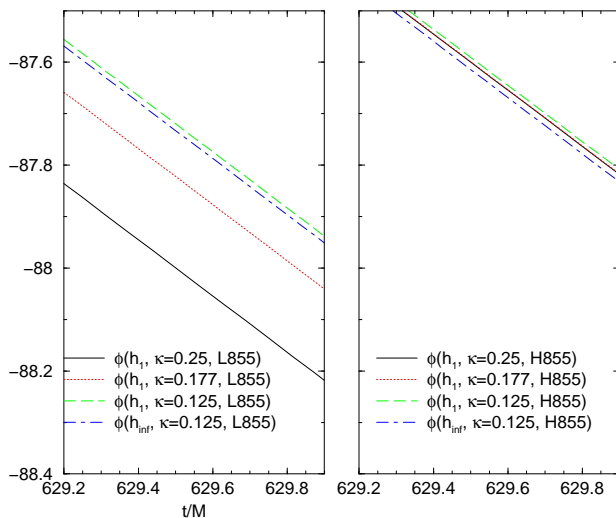


FIG. 14: The phase of the $(\ell = 2, m = 2)$ mode of ψ_4 during the ringdown phase. Shown are phases for the H855 and L855 at three different CFL factors, as well as the Richardson extrapolation phase based on the highest resolution runs with the smallest CFL. Note how the phase converges to different values depending on CFL for the L855 system, but shows consistency between CFL values for the H855 algorithm.

either H855 or H677 if we assume that the error in the phases is given by the differences between the two highest resolutions. However, we note that in all the cases, the phase is not a monotonic function of the resolution, i.e. there are oscillations of the phase. The differences between the phases for H855 and H877 and H855 and H677 are better measures of the error. In this case, we find that the phase error is closer to 0.05. We plot the difference of the highest resolution H855 simulation with the highest resolution H877 and H677 simulations in Fig. 18. Note that, based on the differences between the H855 and H677 simulations, we predict a phase error, during ring-down, of 0.015 rad. (0.045 if we use H877). Interestingly, this lower number is very close to the difference between the H855 Z4 simulations (described below) and the H855 simulations (see Fig. 21). We note that in [75], where the SPEC code was used to compare waveforms using the same evolution system, but different initial data techniques, the waveform phases agreed to within ~ 0.002 rad, which was lower than the estimated overall waveform error of ~ 0.01 rad over a 4000M inspiral.

We also noticed differences in the phase between the ET_2011_10 (and later) version of CARPET (see [63]) and the ET_2011_05 (and previous) versions. In Fig. 19, we use “hg” and “git” to denote the newer and older versions, respectively. As seen in Fig. 19, the differences converge away rapidly with resolution. The source of the deviation appears to be a difference in the prolongation operators that affects non smooth data. The exponentially growing error in the phase apparent during the late inspiral is one of the main reasons why obtaining highly-accurate phases is so difficult.

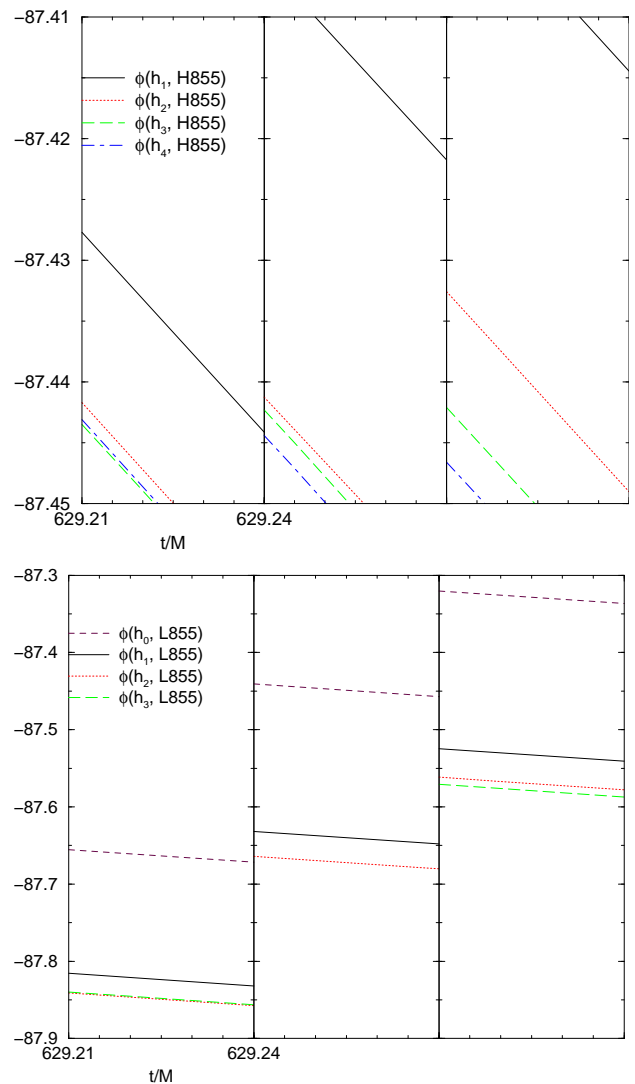


FIG. 15: Plot showing the phase for a short duration during ringdown for simulations using the H855 (top) and L855 (bottom) algorithms. The plots are arranged according to CFL factor κ with $\kappa = 1/4$ on the left, $\kappa = 1/(4\sqrt{2})$ in the middle, and $\kappa = 1/8$ on the right. In each case, the x and y axes are the same for each panel for a given algorithm. For the H855 runs, note that $\kappa = 1/4$ curves are not in convergence order, while $\kappa = 1/(4\sqrt{2})$ are in convergence order but the curve separations are not consistent with convergence. $\kappa = 1/8$ shows convergence, but the extrapolation is about 0.13 rad from the high resolution run which is much larger than expected. The L855 show apparently better convergence properties but the phases are not convergent to each other.

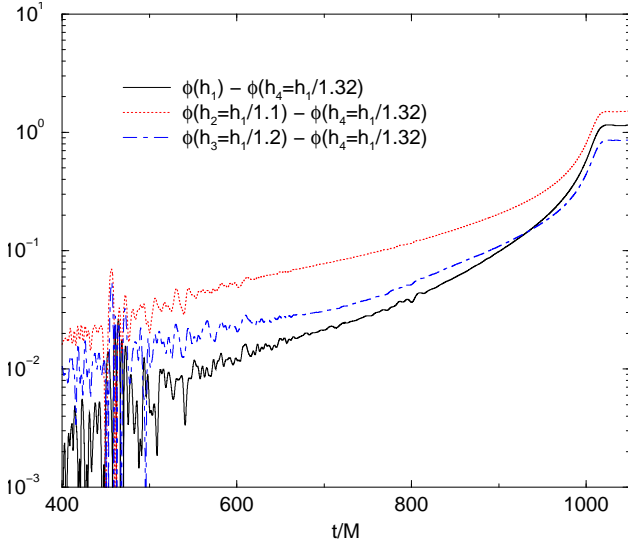


FIG. 16: A plot showing the phase differences between three resolutions of a $q = 1/10$ nonspinning BHB and the corresponding phase for a still higher resolution using the L855 system (with $\kappa = 1/4$). Note how the lowest resolution run has phase closest to the highest resolution for the inspiral phase.

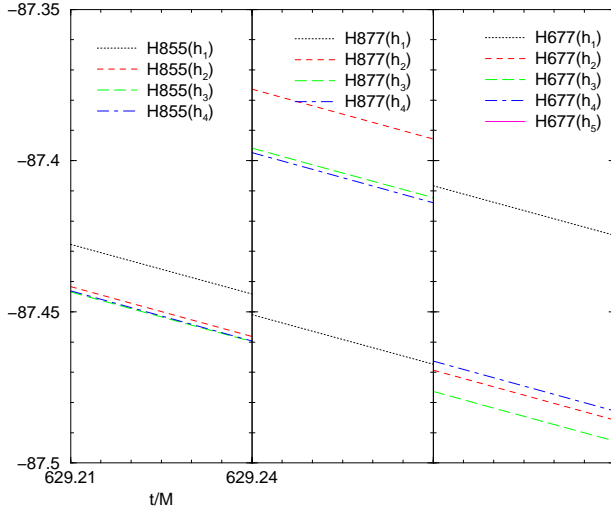


FIG. 17: The phase of the $(\ell = 2, m = 2)$ mode of ψ_4 near merger for the H855, H877, and H677 systems. Note how the more *accurate* H877 and H677 runs actually show significantly more scatter at lower resolutions than H855. For both H877 and H855, the phases for the h_3 and h_4 resolution lie nearly on top of each other. Given the phase differences with the other resolutions, this is likely due to an oscillation (i.e., nonmonotonic dependence) in the phase with resolution.

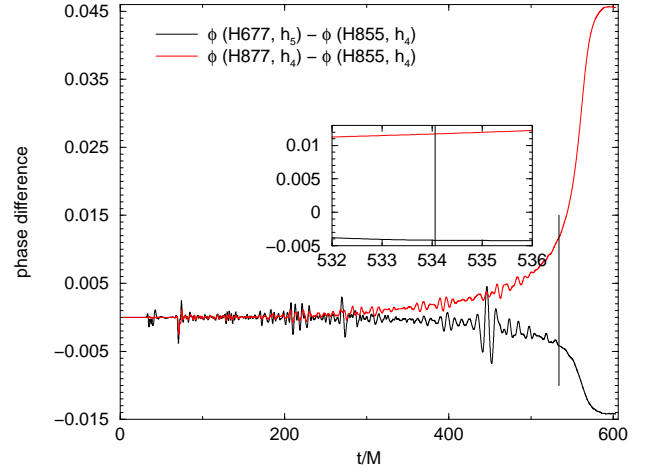


FIG. 18: The difference between the phase of the $(\ell = 2, m = 2)$ mode of ψ_4 as calculated using the H855 and H877, as well as the H855 and H677 systems. The vertical line corresponds to the time when the waveform frequency is $M\omega = 0.2$. At this time, the phase error appears to be as small as 0.005 (0.012, if we use the differences between H855 and H877) rad. Given the results apparent in Fig. 17, we estimate this to be a reasonable error of the phase error.

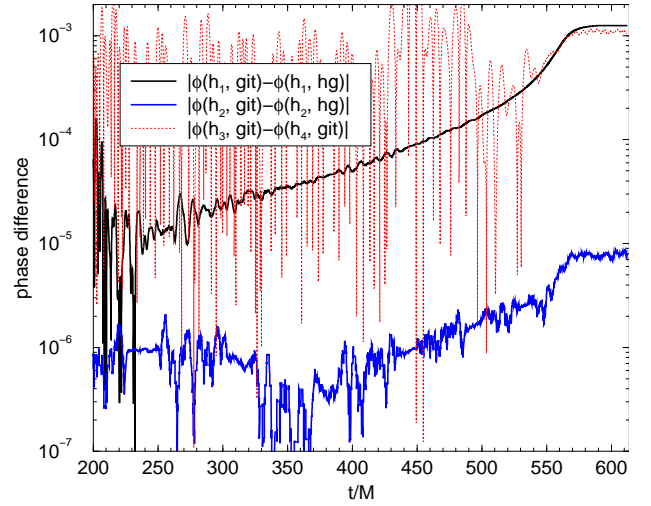


FIG. 19: The phase of the $(\ell = 2, m = 2)$ mode of ψ_4 near merger for the H855 systems with a CFL of $\kappa = 0.25$ using both the git and hg versions of the CARPET AMR driver. The phase deviation between the git and hg versions increases exponentially with time, but decreases rapidly with increasing resolution. For comparison, the phase difference between the medium and high resolutions runs is also shown.

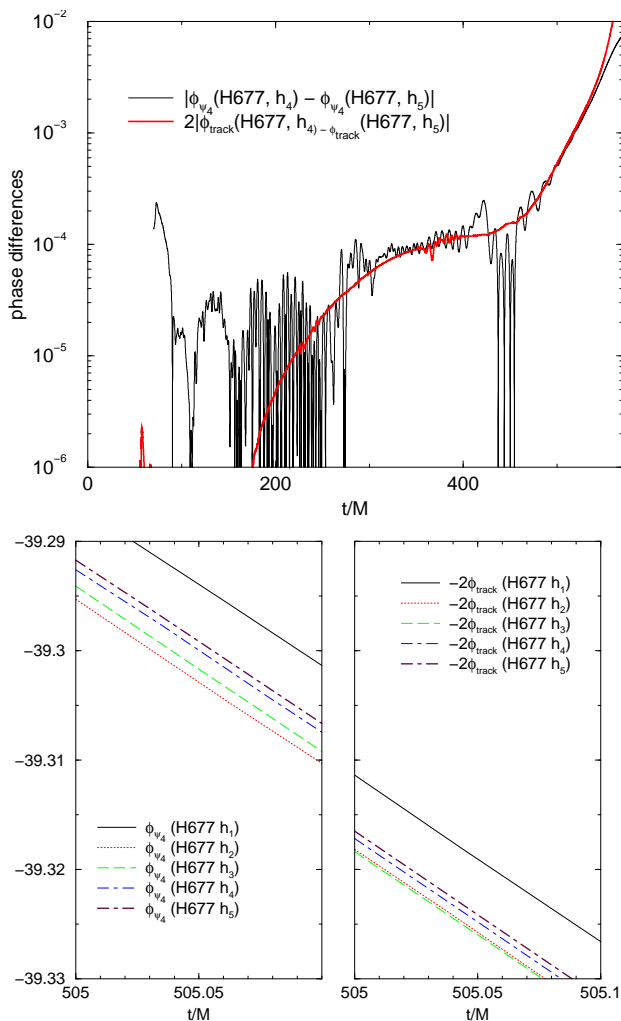


FIG. 20: A comparison of the phase differences in both the trajectory and waveform between the two highest resolutions for the H677 system. The plot ends at the point where the orbital separation is $0.05M$. The agreement between the two curves indicates that the error in the phase of the waveform is associated with the error in the phase of the trajectory. The bottom plot shows the orbital and waveform phases in a small time interval for the different resolutions. Note how the oscillation (with resolution) in the phase of the waveform are matched by similar oscillations in the orbital phase.

F. Convergence of the Amplitude

We measure the amplitude variation with resolution, relative to the highest resolution, of the $(\ell = 2, m = 2)$ mode of ψ_4

$$\delta_i^{\text{amp}} = (|\psi_4|(h_i) - |\psi_4|(h_4)) / |\psi_4|(h_4)$$

for the $\kappa = 0.25, 0.177, 0.125$ H855 configurations. We find that the deviations are smallest for $\kappa = 0.25$, larger for $\kappa = 0.177$, and largest for $\kappa = 0.125$. Interestingly,

To conclude this section, we mention that the phase error seen in the waveform is not a result of the extraction technique, but is rather associated with phase error in the orbital motion itself. This is demonstrated in Fig. 20, where oscillations in phase (with resolution) are apparent in both the orbital phase and waveform phase at the same time.

E. Analysis using the CCZ4 Formalism

The waveforms do not appear to converge in a consistent manner at high resolutions. In order to try to elucidate the origin of this problem, we repeated several of the simulations using the Conformal Z4 algorithm developed in Alic *et al* [77]. For the Z_4 parameters, we used $\kappa_1 = 0.1$, $\kappa_2 = 0$, and $\kappa_3 = 0$ (Alic *et al* suggest setting $\kappa_3 = 1/2$, but our simulations were based on an earlier version of their paper). We used the LAZEV coding infrastructure to generate the Z4 evolution code. In addition, we modified the gauge conditions to use Eq. (3) above (with $\tilde{\Gamma}^i$ replaced by the CCZ4 variable $\hat{\Gamma}^i$), rather than the gauge condition used in [77] (for the damping parameters, we used the values given in [77]). For these Z4 runs, we used the H855 system, that is, eighth-order centered finite differencing, fifth-order dissipation, fifth-order spatial prolongation, a full complement of 16 buffer zones, and fourth-order accurate initialization. As is evident in Fig. 21, for a given spatial resolution, the Z4 algorithm exhibits a larger truncation error compared to BSSN. While the Z4 runs show better than 4th-order convergence, with clean convergence at all resolutions attempted, the size of the error makes comparison with BSSN difficult. That is, with coarser resolutions, the BSSN algorithm also appears to be cleanly convergent. Nevertheless, we use a Richardson extrapolation of the waveform phase for Z4 and compare this extrapolated phase with the BSSN phases, as shown in Fig. 21. Here the BSSN phases are all much closer to the extrapolated Z4 phase than any of the individual Z4 phases. It would thus appear that the Z4 and BSSN results are consistent.

the $\kappa = 0.177$ results are more noisy than either of the other two. As shown in Fig. 22, clear convergence is seen for the $\kappa = 0.125$ configurations, while an oscillation is seen in the $\kappa = 0.25$ results, which is consistent with our previous findings for the phase errors. That is, while cleaner convergence is seen with $\kappa = 0.125$, this appears to be a consequence of the larger error associated with smaller CFLs. Thus, for high accuracy runs, one should apparently not use $\kappa = 0.125$. The overall relative amplitude error appears to be controllable to within 0.1%.

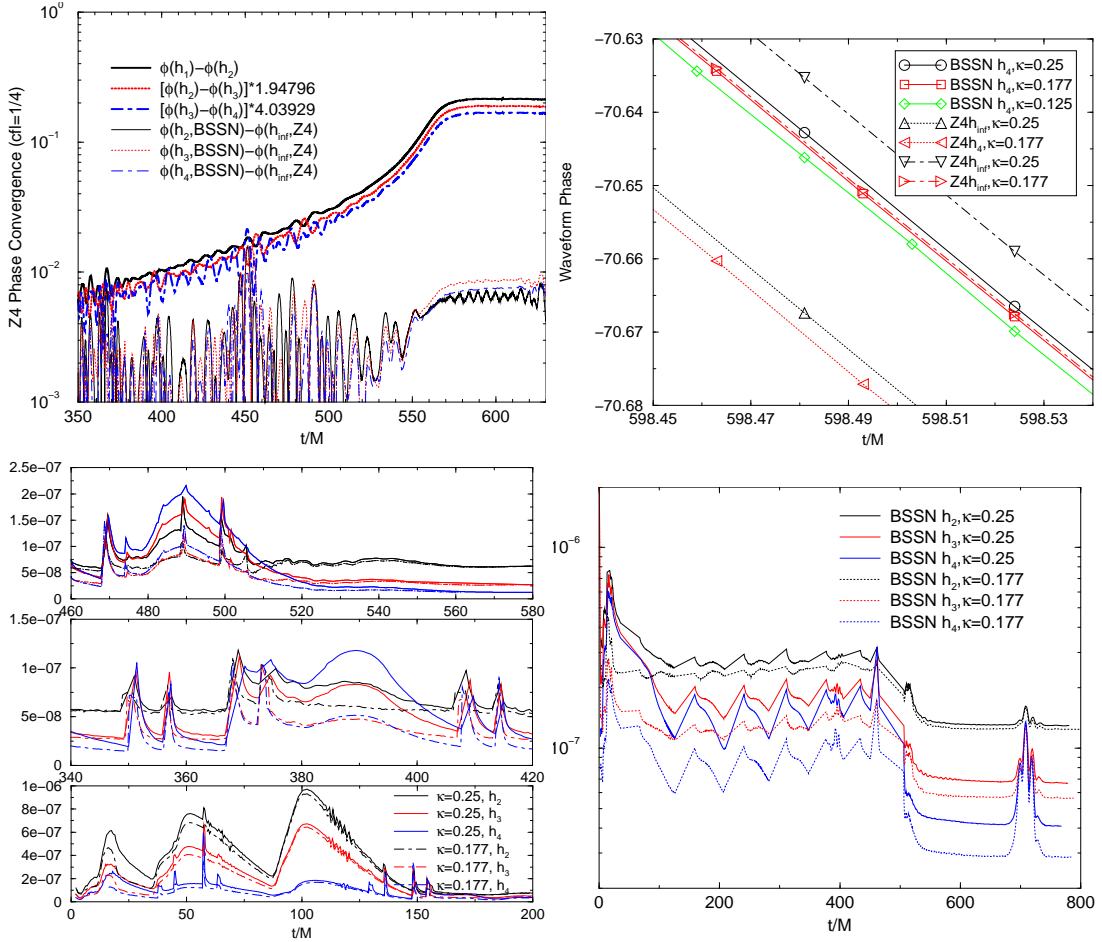


FIG. 21: (top left) The phase convergence for the Z4 evolutions and a comparison with the Richardson extrapolated phase from the Z4 evolutions with the corresponding BSSN phases. (top right) The waveform phase during the late ringdown. The BSSN phases all lie between the highest resolution Z4 phases and the extrapolated phases. However, there also seems to be a trend towards moving to more negative phases as the CFL is reduced. This is observable in both BSSN and Z4. (bottom left) The L_2 norm of the Hamiltonian constraint for the Z4 runs with 2 different CFLs. Convergence with resolution and consistency between CFLs is apparent at early and late times. However, inconsistencies between CFLs and nonconvergent behavior is apparent in the later inspiral and merger phases. The oscillations in $\|\mathcal{H}\|_2$ during the inspiral are consistent with the findings of [77]. (bottom right) The L_2 norm of the Hamiltonian constraint for the comparable BSSN runs. Here improvements in the CFL are apparent when increasing resolution and decreasing the CFL factor. (Note that the spikes apparent in Fig. 5 have been removed for clarity.)

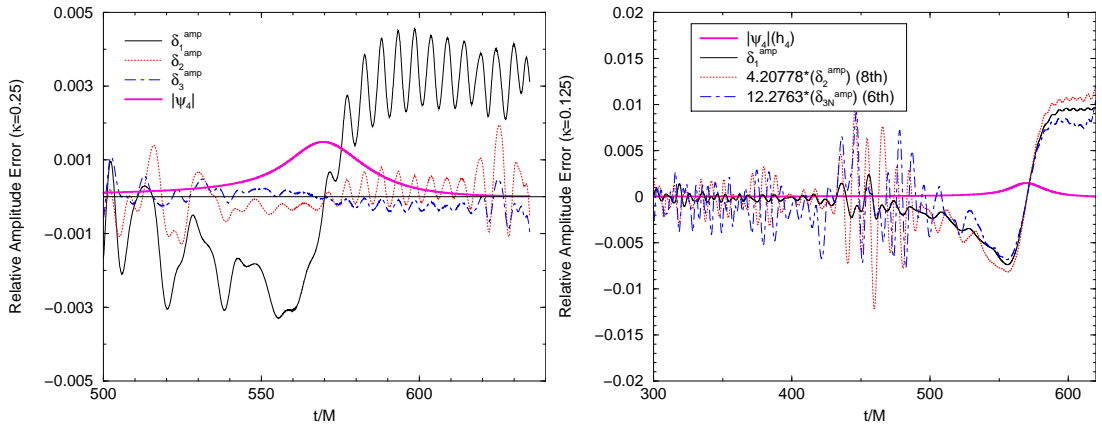


FIG. 22: The error in the amplitude δ_i^{amp} of the $(\ell = 2, m = 2)$ mode of ψ_4 [$\delta_i^{\text{amp}} = (|\psi_4|(h_i) - |\psi_4|(h_4))/|\psi_4|(h_4)$]. Clean convergence is seen for the $\kappa = 0.125$ runs, while a change in sign in δ_3 is seen in the $\kappa = 0.25$ runs. The magnitude of δ_3 is roughly a factor of 3 smaller for the $\kappa = 0.25$ runs.

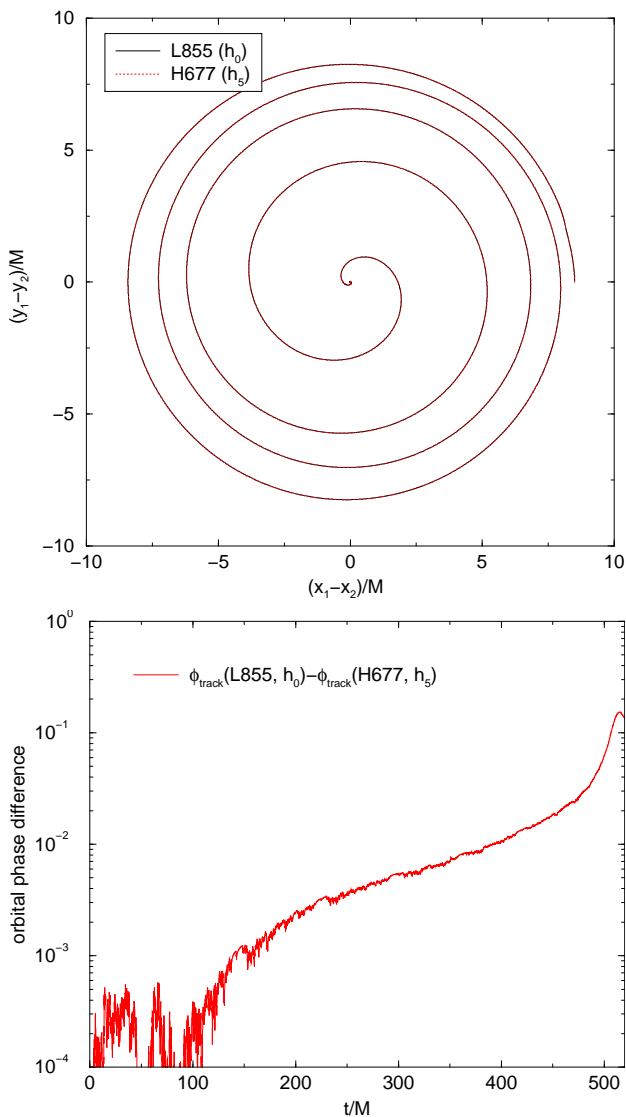


FIG. 23: A comparison of the orbital trajectory for the lowest resolution L877 (low-accuracy) simulation and the highest resolution H677 simulation. The phase error at merger is 0.15 rad, which corresponds to a waveform phase error of 0.30 rad. The actual post-merger phase difference is about 0.20 rad.

We conclude this section by noting that even the lowest accuracy L855 simulation is accurate enough for many applications where extreme phase accuracy is not needed (e.g. recoil studies). In Fig. 23 we show the orbital trajectory for the lowest resolution L855 and highest resolution H677 simulations. The two orbital trajectories overlap throughout the entire simulation, even at merger, where the phase error increases to 0.15 rad.

Finally, we note that our AMR grids changed with resolution because our chosen radii fell in between actual gridpoints. This means that the AMR boundary sizes changed from resolution to resolution. In fact, the location of the AMR levels was determined during each evolution by tracking the location of the ‘‘puncture’’. This

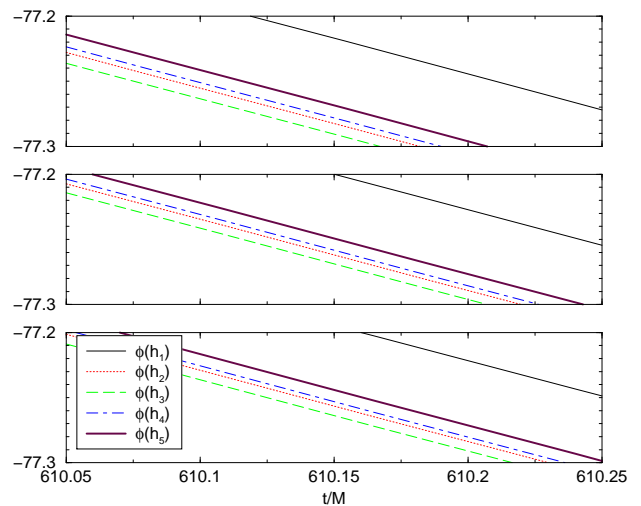


FIG. 24: The phase of the $(\ell = 2, m = 2)$ mode of ψ_4 as calculated at $r = 50M$ (bottom) and $r = 60M$ (middle) and $r = 100M$ (top) for the H677 system. The $r = 50M$ and $r = 100M$ spheres intersect two AMR levels, while the $r = 60M$ lies on a single level (but does intersect a buffer region). No difference in the oscillations in the phases of the waveform are apparent.

means that the AMR locations also changed from resolution to resolution. In addition, our $r = 50$ waveform was generated by integrating over a sphere that crossed AMR boundaries. While it is difficult to determine the effect of the former on our results, we can show that the latter effect (due to integrating over AMR boundaries) was not a significant source of error. In Fig. 24, we plot the phase from the five H677 simulations at both $r = 50$ and $r = 100$ (the plots have been translated). Note how the oscillations in the phase at $r = 50$ are mirrored in the phase at $r = 100$.

IV. DISCUSSION

After removing various low-accuracy approximations, we were able to reduce variation in the horizon mass of the two BHs in a BHB to the level of $10^{-6}M$. We find the Hamiltonian constraint violations (both the L_2 norm in the bulk, and horizon-averaged values) are convergent. The momentum and BSSN constraints also converge to fourth-order on the horizons. Convergence of the momentum constraint in the bulk is less clear, with only H677 showing clean convergence.

We find a stochastic error in the phase of the waveform that prevents us from seeing convergence at high resolution. We speculate that this stochastic error is associated with the high-frequency, unresolved, wave from the initial-data burst of radiation that reflects off the AMR boundaries, producing a complex, highly-variable interference pattern on the grid (see Fig. 1). Without a clean convergence of the high-resolution runs, it is difficult to predict the actual error in the phase of the waveform at merger and ringdown. We note that the oscillations in the phase (with resolution) appear to be controllable to about the level of 0.015 rad., which is accurate enough for data analysis purposes (i.e. exceeds NRAR and NINJA accuracy goals). Whether the phase error really is this small depends on the source of the oscillations. If these are due to essentially stochastic errors introduced by grid reflections, then it seems reasonable to assume the phase error is controllable to 0.015 rad. However, if the source of the oscillation is actually lower-order errors becoming more dominant at higher resolutions, then we need far higher-resolution runs. Since the lowest-order error is the second-order prolongation (in time) error, one may need to perform a convergence study (at very high resolutions) where the grids are refined by factors of two between resolutions (with coarsest resolution as fine, or finer than, our finest resolution). Such a study would be computationally very expensive, but may ultimately be necessary.

One reason why grid refinement boundaries may be a significant issue has to do with reflection of the (relatively) high-frequency initial burst of radiation. By construction, the AMR grids are well adapted to evolving the relatively low-frequency waveform signal (with smallest period of about $10M$), but the initial burst has frequencies a factor of four higher. To properly evolve this pulse, may require a factor of four increase in resolution, which would require a factor of 256 in computational resources. Fortunately, this signal is not physical, and one only needs to confirm that the effects on the rest of the waveform of poorly resolving this pulse are within data analysis tolerances. However, use of data with smaller spurious high-frequency wave content [78, 79] and more correct low-frequency wave content [80–82] should help reduce AMR reflections and the corresponding stochastic phase error. We expect to recover full convergence of the moving puncture formalism in the unigrid limit performing tests similar to those in Ref. [83].

In order to obtain an independent measure of the phase error in our simulations, we compare the phase of the waveform obtained using both the BSSN and CCZ4 formalisms. We find agreement at the level of 0.01 radian, but only after a Richardson extrapolation. Because both codes used very similar technologies and the same AMR implementation, it would be very useful to compare the results from these simulations with other codes, analogous to what was done with the Samurai project [84]. Comparisons with other AMR-based codes, such as BAM [53], and pseudospectral codes, such as SPEC [85, 86], would be especially useful.

Our simulations show that the L855 system is inappropriate for use where high phase-accuracy is needed. However, for situations where lower accuracy is acceptable, e.g. for recoil studies, it can be used. Our tests also show that, even when using high-accuracy methods with a state-of-the-art AMR code for numerical relativity, clean convergence remains elusive, but we have seen improvements with the prolongation order in systems such as H677 and H877, with signs of consistency for H677. We note that [71] use the numerically more expensive H899 algorithm, which also includes upwinded finite differencing stencils. They found that upwinding increases the accuracy of the simulation.

V. CONCLUSION

We analyze the accuracy of a BHB simulation by examining the preservation of the individual horizon masses, convergence of the constraints, and convergence of the magnitude and phase of the ($\ell = 2, m = 2$) mode ψ_4 extracted at $r = 50M$. As seen in Fig. 2, the fast, but low-accuracy approximations lead to poor conservation of the mass compared to the slower, but more accurate, techniques. For the high-accuracy techniques, we find convergence of the constraints to the expected order, as seen in Fig. 5. A residual, possibly stochastic, phase error is seen in the waveform itself. By comparing the waveforms generated using different techniques and different evolution systems, as shown in Figs. 18 and 21, we find consistency in the phase at the level of 0.05 rad. over the entire waveform.

Acknowledgments

The authors thank D.Alic, I.Hinder, F. Löffler, C.Palenzuela, and Z.Etienne for helpful discussions. We gratefully acknowledge the NSF for financial support from Grants AST-1028087, PHY-0929114, PHY-0969855, PHY-0903782, OCI-0832606, PHY-1229173, PHY-1212426, and DRL-1136221, and NASA for financial support from Grant No. 07-ATFP07-0158. Computational resources were provided by the Ranger system at the Texas Advance Computing Center (Teragrid allocation TG-PHY060027N), which is supported in part

by the NSF, and by NewHorizons at Rochester Institute of Technology, which was supported by NSF grant No.

PHY-0722703, PHY-1229173, DMS-0820923, and AST-1028087.

-
- [1] F. Pretorius, *Phys. Rev. Lett.* **95**, 121101 (2005), gr-qc/0507014.
- [2] M. Campanelli, C. O. Lousto, P. Marronetti, and Y. Zlochower, *Phys. Rev. Lett.* **96**, 111101 (2006), gr-qc/0511048.
- [3] J. G. Baker, J. Centrella, D.-I. Choi, M. Koppitz, and J. van Meter, *Phys. Rev. Lett.* **96**, 111102 (2006), gr-qc/0511103.
- [4] B. Aylott et al., *Class. Quant. Grav.* **26**, 165008 (2009), 0901.4399.
- [5] B. Aylott et al., *Class. Quant. Grav.* **26**, 114008 (2009), 0905.4227.
- [6] F. Herrmann, D. Shoemaker, and P. Laguna, *AIP Conf.* **873**, 89 (2006), gr-qc/0601026.
- [7] J. G. Baker et al., *Astrophys. J.* **653**, L93 (2006), astro-ph/0603204.
- [8] J. A. González, U. Sperhake, B. Bruggmann, M. Hannam, and S. Husa, *Phys. Rev. Lett.* **98**, 091101 (2007), gr-qc/0610154.
- [9] F. Herrmann, I. Hinder, D. Shoemaker, P. Laguna, and R. A. Matzner, *Astrophys. J.* **661**, 430 (2007), gr-qc/0701143.
- [10] M. Campanelli, C. O. Lousto, Y. Zlochower, and D. Merritt, *Astrophys. J.* **659**, L5 (2007), gr-qc/0701164.
- [11] M. Campanelli, C. O. Lousto, Y. Zlochower, and D. Merritt, *Phys. Rev. Lett.* **98**, 231102 (2007), gr-qc/0702133.
- [12] C. O. Lousto and Y. Zlochower, *Phys. Rev.* **D79**, 064018 (2009), 0805.0159.
- [13] D. Pollney et al., *Phys. Rev.* **D76**, 124002 (2007), 0707.2559.
- [14] J. A. González, M. D. Hannam, U. Sperhake, B. Bruggmann, and S. Husa, *Phys. Rev. Lett.* **98**, 231101 (2007), gr-qc/0702052.
- [15] B. Bruggmann, J. A. Gonzalez, M. Hannam, S. Husa, and U. Sperhake, *Phys. Rev.* **D77**, 124047 (2008), 0707.0135.
- [16] D.-I. Choi et al., *Phys. Rev.* **D76**, 104026 (2007), gr-qc/0702016.
- [17] J. G. Baker et al., *Astrophys. J.* **668**, 1140 (2007), astro-ph/0702390.
- [18] J. D. Schnittman et al., *Phys. Rev.* **D77**, 044031 (2008), 0707.0301.
- [19] J. G. Baker et al., *Astrophys. J.* **682**, L29 (2008), 0802.0416.
- [20] J. Healy et al., *Phys. Rev. Lett.* **102**, 041101 (2009), 0807.3292.
- [21] F. Herrmann, I. Hinder, D. Shoemaker, and P. Laguna, *Class. Quant. Grav.* **24**, S33 (2007).
- [22] F. Herrmann, I. Hinder, D. M. Shoemaker, P. Laguna, and R. A. Matzner, *Phys. Rev.* **D76**, 084032 (2007), 0706.2541.
- [23] W. Tichy and P. Marronetti, *Phys. Rev.* **D76**, 061502 (2007), gr-qc/0703075.
- [24] M. Koppitz, D. Pollney, C. Reisswig, L. Rezzolla, J. Thornburg, et al., *Phys. Rev. Lett.* **99**, 041102 (2007), gr-qc/0701163.
- [25] S. H. Miller and R. A. Matzner, *Gen. Rel. Grav.* **41**, 525 (2009), 0807.3028.
- [26] C. O. Lousto and Y. Zlochower, *Phys. Rev. Lett.* **107**, 231102 (2011), 1108.2009.
- [27] Y. Zlochower, M. Campanelli, and C. O. Lousto, *Class. Quant. Grav.* **28**, 114015 (2011), 1011.2210.
- [28] C. O. Lousto and Y. Zlochower, *Phys. Rev.* **D83**, 024003 (2011), 1011.0593.
- [29] C. O. Lousto, Y. Zlochower, M. Dotti, and M. Volonteri, *Phys. Rev.* **D85**, 084015 (2012), 1201.1923.
- [30] Y. Sekiguchi and M. Shibata, *Astrophys. J.* **737**, 6 (2011), 1009.5303.
- [31] Z. B. Etienne, Y. T. Liu, V. Paschalidis, and S. L. Shapiro, *Phys. Rev.* **D85**, 064029 (2012), 1112.0568.
- [32] Z. B. Etienne, Y. T. Liu, S. L. Shapiro, and T. W. Baumgarte, *Phys. Rev. D* **79**, 044024 (2009), 0812.2245.
- [33] Z. B. Etienne, J. A. Faber, Y. T. Liu, S. L. Shapiro, K. Taniguchi, and T. W. Baumgarte, *Phys. Rev. D* **77**, 084002 (2008), arXiv:0712.2460 [astro-ph].
- [34] L. Rezzolla, B. Giacomazzo, L. Baiotti, J. Granot, C. Kouveliotou, et al., *Astrophys. J.* **732**, L6 (2011), 1101.4298.
- [35] K. Hotokezaka, K. Kyutoku, H. Okawa, M. Shibata, and K. Kiuchi, *Phys. Rev.* **D83**, 124008 (2011), 1105.4370.
- [36] Y. Sekiguchi, K. Kiuchi, K. Kyutoku, and M. Shibata, *Phys. Rev. Lett.* **107**, 051102 (2011), 1105.2125.
- [37] F. Foucart, M. D. Duez, L. E. Kidder, M. A. Scheel, B. Szilagyi, et al., *Phys. Rev.* **D85**, 044015 (2012), 11 pages, 11 figures - Updated to match published version, 1111.1677.
- [38] M. D. Duez, F. Foucart, L. E. Kidder, H. P. Pfeiffer, M. A. Scheel, et al., *Phys. Rev.* **D78**, 104015 (2008), 0809.0002.
- [39] C. O. Lousto and Y. Zlochower, *Phys. Rev.* **D77**, 024034 (2008), 0711.1165.
- [40] M. Campanelli, C. O. Lousto, and Y. Zlochower, *Phys. Rev.* **D77**, 101501(R) (2008), 0710.0879.
- [41] P. Galaviz and B. Brueggemann, *Phys. Rev.* **D83**, 084013 (2011), 1012.4423.
- [42] M. Campanelli, C. O. Lousto, and Y. Zlochower, *Phys. Rev.* **D79**, 084012 (2009), 0811.3006.
- [43] R. Owen, *Phys. Rev.* **D81**, 124042 (2010), 1004.3768.
- [44] M. Campanelli, C. O. Lousto, and Y. Zlochower, *Phys. Rev.* **D74**, 041501(R) (2006), gr-qc/0604012.
- [45] M. Ponce, C. Lousto, and Y. Zlochower, *Class. Quant. Grav.* **28**, 145027 (2011), 1008.2761.
- [46] M. Shibata and H. Yoshino, *Phys. Rev.* **D81**, 104035 (2010), 1004.4970.
- [47] M. Zilhao, H. Witek, U. Sperhake, V. Cardoso, L. Gualtieri, et al., *Phys. Rev.* **D81**, 084052 (2010), 1001.2302.
- [48] H. Witek, M. Zilhao, L. Gualtieri, V. Cardoso, C. Herdeiro, et al., *Phys. Rev.* **D82**, 104014 (2010), 1006.3081.
- [49] C. O. Lousto and Y. Zlochower, *Phys. Rev. Lett.* **106**, 041101 (2011), 1009.0292.
- [50] U. Sperhake, V. Cardoso, C. D. Ott, E. Schnetter, and H. Witek, *Phys. Rev.* **D84**, 084038 (2011), 1105.5391.
- [51] G. Lovelace, M. A. Scheel, and B. Szilagyi, *Phys. Rev.*

- D83**, 024010 (2011), 1010.2777.
- [52] G. Lovelace, M. Boyle, M. A. Scheel, and B. Szilagyi, *Class. Quant. Grav.* **29**, 045003 (2012), 1110.2229.
- [53] B. Brügmann et al., *Phys. Rev.* **D77**, 024027 (2008), gr-qc/0610128.
- [54] M. Ansorg, B. Brügmann, and W. Tichy, *Phys. Rev.* **D70**, 064011 (2004), gr-qc/0404056.
- [55] S. Brandt and B. Brügmann, *Phys. Rev. Lett.* **78**, 3606 (1997), gr-qc/9703066.
- [56] J. M. Bowen and J. W. York, Jr., *Phys. Rev.* **D21**, 2047 (1980).
- [57] Y. Zlochower, J. G. Baker, M. Campanelli, and C. O. Lousto, *Phys. Rev.* **D72**, 024021 (2005), gr-qc/0505055.
- [58] P. Marronetti, W. Tichy, B. Brügmann, J. Gonzalez, and U. Sperhake, *Phys. Rev.* **D77**, 064010 (2008), 0709.2160.
- [59] T. Nakamura, K. Oohara, and Y. Kojima, *Prog. Theor. Phys. Suppl.* **90**, 1 (1987).
- [60] M. Shibata and T. Nakamura, *Phys. Rev.* **D52**, 5428 (1995).
- [61] T. W. Baumgarte and S. L. Shapiro, *Phys. Rev.* **D59**, 024007 (1999), gr-qc/9810065.
- [62] Cactus Computational Toolkit home page: <http://cactuscode.org>.
- [63] Einstein Toolkit home page: <http://einsteintoolkit.org>.
- [64] F. Löffler, J. Faber, E. Bentivegna, T. Bode, P. Diener, et al., *Class. Quant. Grav.* **29**, 115001 (2012), 1111.3344.
- [65] E. Schnetter, S. H. Hawley, and I. Hawke, *Class. Quant. Grav.* **21**, 1465 (2004), gr-qc/0310042.
- [66] J. Thornburg, *Class. Quant. Grav.* **21**, 743 (2004), gr-qc/0306056.
- [67] O. Dreyer, B. Krishnan, D. Shoemaker, and E. Schnetter, *Phys. Rev.* **D67**, 024018 (2003), gr-qc/0206008.
- [68] M. Alcubierre, B. Brügmann, P. Diener, M. Koppitz, D. Pollney, E. Seidel, and R. Takahashi, *Phys. Rev.* **D67**, 084023 (2003), gr-qc/0206072.
- [69] J. R. van Meter, J. G. Baker, M. Koppitz, and D.-I. Choi, *Phys. Rev.* **D73**, 124011 (2006), gr-qc/0605030.
- [70] E. Schnetter, *Class. Quant. Grav.* **27**, 167001 (2010), 1003.0859.
- [71] D. Pollney, C. Reisswig, E. Schnetter, N. Dorband, and P. Diener, *Phys. Rev.* **D83**, 044045 (2011), 0910.3803.
- [72] B. Szilagyi, L. Lindblom, and M. A. Scheel, *Phys. Rev.* **D80**, 124010 (2009), 0909.3557.
- [73] M. Babiuc, B. Szilagyi, J. Winicour, and Y. Zlochower, *Phys. Rev.* **D84**, 044057 (2011), 1011.4223.
- [74] C. Reisswig, N. T. Bishop, D. Pollney, and B. Szilagyi, *Phys. Rev. Lett.* **103**, 221101 (2009), 0907.2637.
- [75] B. Garcia, G. Lovelace, L. E. Kidder, M. Boyle, S. A. Teukolsky, et al., *Phys. Rev.* **D86**, 084054 (2012), 1206.2943.
- [76] H. Nakano, Y. Zlochower, C. O. Lousto, and M. Campanelli, *Phys. Rev.* **D84**, 124006 (2011), 1108.4421.
- [77] D. Alic, C. Bona-Casas, C. Bona, L. Rezzolla, and C. Palenzuela, *Phys. Rev.* **D85**, 064040 (2012), 1106.2254.
- [78] M. Hannam, S. Husa, B. Brügmann, J. A. Gonzalez, and U. Sperhake, *Class. Quant. Grav.* **24**, S15 (2007), gr-qc/0612001.
- [79] G. Lovelace, *Class. Quant. Grav.* **26**, 114002 (2009), 0812.3132.
- [80] B. C. Mundim, B. J. Kelly, Y. Zlochower, H. Nakano, and M. Campanelli, *Class. Quant. Grav.* **28**, 134003 (2011), 1012.0886.
- [81] B. J. Kelly, W. Tichy, Y. Zlochower, M. Campanelli, and B. F. Whiting, *Class. Quant. Grav.* **27**, 114005 (2010), 0912.5311.
- [82] B. J. Kelly, W. Tichy, M. Campanelli, and B. F. Whiting, *Phys. Rev.* **D76**, 024008 (2007), 0704.0628.
- [83] M. C. Babiuc et al., *Class. Quant. Grav.* **25**, 125012 (2008), 0709.3559.
- [84] M. Hannam et al., *Phys. Rev.* **D79**, 084025 (2009), 0901.2437.
- [85] M. A. Scheel et al., *Phys. Rev.* **D74**, 104006 (2006), gr-qc/0607056.
- [86] M. Boyle, L. Lindblom, H. Pfeiffer, M. Scheel, and L. E. Kidder, *Phys. Rev.* **D75**, 024006 (2007), gr-qc/0609047.